Experimental Investigation of Capillary Performance of Additively-Manufactured Lattice Specimen for Fluid Wicking Applications

Center for Advanced Manufacturing in Space Technology & Applied Research (CAM-STAR)
University of the District of Columbia, Washington D.C., USA

Presented By
Jiajun Xu, Ph.D., P.E.

Thermal & Fluids Analysis Workshop
TFAWS 2023
August 21-25, 2023
NASA Goddard Space Flight Center
College Park, MD

Motivation

Additive manufacturing (AM) and its advent has introduced many design solutions and concepts to the engineer which were inconceivable prior to AM.

Many disciplines of science and engineering are leveraging these capabilities. One of which is in thermofluidic applications since AM can print much more complex structures than conventional means.

Lattice structures have been a major focus with these rapidly evolving capabilities. With many applications showing promise in thermofluidic, generative design, and mechanical loading to name a few

Introduction

- Wick structures play a crucial role in performance of passive two-phase thermal management systems. (e.g., heat pipes, vapor chambers, cold plates, etc.) [1-5]

- The wick structure functions as a pump for fluid flow to keep it recirculated in the system using capillary-driven liquid motion within the micropores.

- Rapidly evolving AM technologies have become a focus of interest in fabricating metallic wick structures with controlled properties

- Additively-manufactured lattice structures provides the capability to design and fabricate microstructures with complex cell topologies and freeform geometries, therefore, it is chosen here to as the starting point of replicating the repeating pattern of certain wick structures

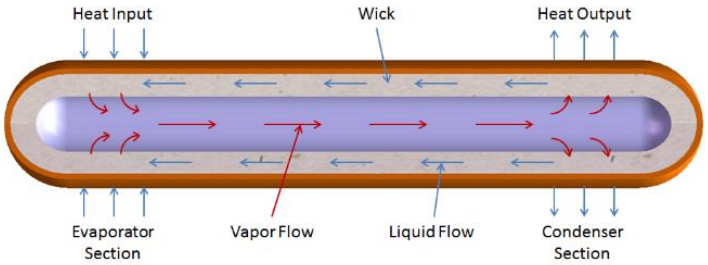

Fig. 1 Schematic displaying the function of a heat pipe

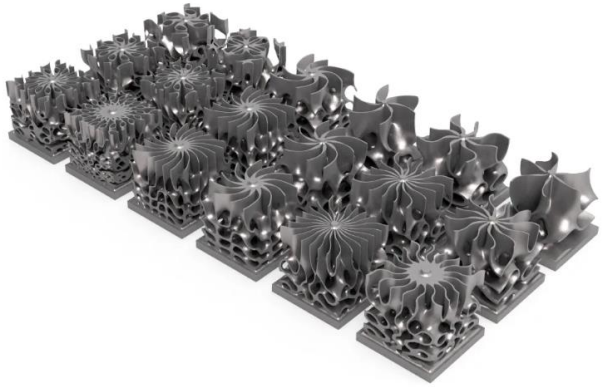

Fig. 2 Generatively designed heat exchangers achieved with nTopology

Introduction

- Rapidly evolving additive manufacturing (AM) technologies, in particular, laser powder bed fusion technologies, have become a focus of interest in fabricating metal lattice structures with controlled properties [5-9].
- One of the principal privileges of additively-manufactured lattice structures is the capability to design and fabricate microstructures with complex cell topologies and freeform geometries which are not feasible using conventional manufacturing techniques.
- Recently, Jafari et al. [5, 6] investigated the feasibility of using selective laser melting (SLM) to additively fabricate lattice structures with CL20ES stainless steel powder. For a range of pore sizes and porosities, they observed that porosity and surface morphology influence the thermophysical properties, capillary performance, and droplet's contact angle on the printed surface.
- In another study, Ameli et al. [10] demonstrated the viability of fabricating sintered aluminum dummy heat pipe samples using the SLM technique with various aluminum wick characteristics built up in a single process with the container, end cap, and fill tube where ammonia is engaged as the working fluid. In this study, porous structures of $15 \times 15 \times 15$ mm3 blocks with octahedral unit cell sizes of 300, 500, and 700 μm were manufactured to measure their porosity and permeability.

Design and Fabrication

- In designing the specimens, the primary parameter of capillary force was the focus. This target point led to design the structures around effective pore radii, the main driving factor for capillary force.

- Strut based lattice structures have many superior properties that foams and honeycombs don't get because of their unique property of tailoring. Thus, the topologies of face centered cubic, body-centered cubic, and octet truss were decided based on their compatibility with minimum build angle and their proven manufacturability. All of which were drafted in nTopology

- The lattice samples in the present study were fabricated in a vertical orientation using the Direct Metal Laser Sintering (DMLS) technique via the EOS M280 configured for MS1 maraging steel.

- The DMLS for the present study applies a laser power of 400 W to sinter a 40-μm-thick layer of metal powder with a scan speed up to 7 m/s.

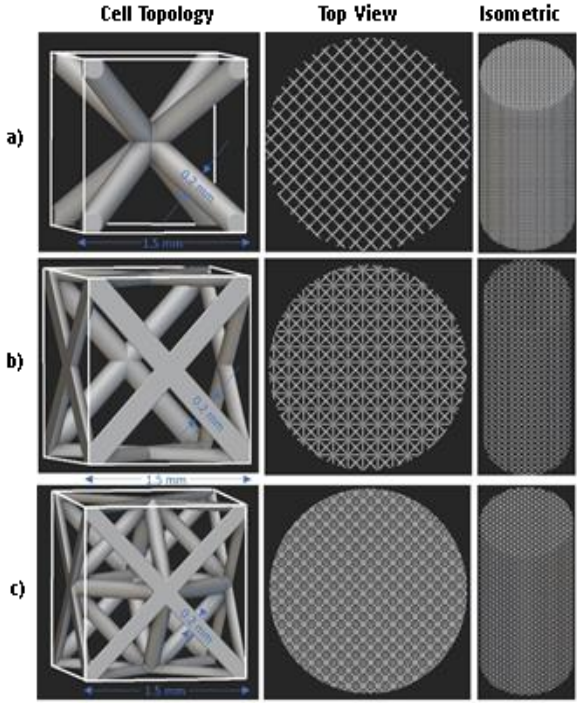

Fig. 4 Representative CAD models of lattice topologies with a unit cell of 1.5 mm and struts of 200-micron thick: a) body-centered cubic (*BS1.5*), b) face-centered cubic (*FS1.5*), and c) octet truss (*OS1.5*).

Lattice Topology (symbol)	Strut Thickness (symbol)	Cell Size (symbol)
Body-centered cubic (**B**)	0.2 mm (**S**)	1 mm (**1**)
Faced-centered cubic (**F**)	0.25 mm (**M**)	1.5 mm (**1.5**)
Octet Truss (**O**)	0.3 mm (**L**)	2 mm (**2**)
Three-Character Labeling Style		
Topology *Symbol* / Strut *Symbol* / Cell *Symbol*		
B/F/O *S/M/L* *1/1.5/2*		

Table 1. Sample labeling guidelines

Fig. 3 Photo depicting the EOS M280

Measuring and Imaging Techniques

- A digital microscope (KEYENCE VHX-7100) was used to capture optical micrographs of the lattice samples.
- Capillary performance experiments were conducted by a rate-of-rise technique according to a procedure addressed by Faghri and Holley to present capillary elevations versus time for methanol.
- An Infrared (IR) camera is utilized to accurately identify the front location of wicked liquid based on the difference in emissivity of the liquid and sample material. The entire set-up is shown in Fig. 5.
- This particular testing method was chosen because it is a passive test. This is crucial since the goal was to examine the capillary pumping mechanism between the lattices and fluid. As well as most applications that wicking structures play critical roles in are passive systems.
- All data from the various instruments was compiled simultaneously using a computer program that interfaced with Excel.

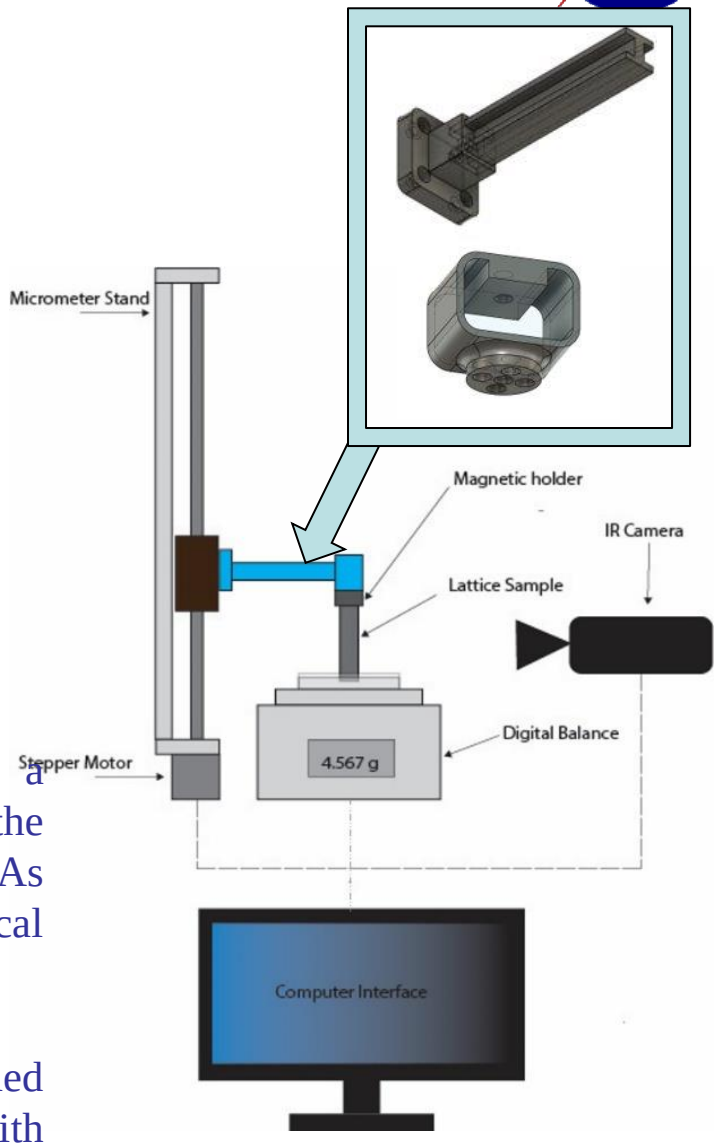

Fig. 5 Schematic of the test apparatus, including Model of assembly of lattice mounting arm

Porosity Measurements

The porosity of each sample is characterized and double-checked using two approaches:

(i) Archimedes approach: the porosity of samples is measured by weighing the amount of methanol required to saturate the wick structure. To conduct the porosity measurements, a precision balance, methanol, and a pipette are employed.

$$\frac{1}{\varepsilon} = 1 + \left(\frac{m_{ls} \cdot \rho_l}{m_l \cdot \rho_{ls}}\right) \qquad \text{Eq. (1)}$$

where ε stands for the porosity, m_{ls} and ml are the masses of dry lattice structure and liquid uptake, respectively, and ρ_{ls} and ρ_l account for densities of the metal powder and methanol liquid, respectively.

(i) direct mass measurement: in this approach, the porosity of each lattice sample is estimated by dividing the mass measured from dry weighing, by the sample volume taken from the measurement of dimensions, and by the bulk or apparent density of the lattice samples. Following this approach, the porosity is calculated as follows:

$$\varepsilon = 1 - \left(\frac{m_{ls}}{\rho_b \cdot V}\right) \qquad \text{Eq. (2)}$$

Where m_{ls} stands for dry mass, ρ_b is apparent density, and V is the sample volume.

Porosity Results

- Fig. 6 represents the porosity data collected and analyzed for the lattice samples of different topologies designed and fabricated in the present study.
- The results consistently reveal higher porosities for the body-centered cubic topology compared to those of the face-centered cubic and octet truss, respectively, for the same unit cell size and the same strut thickness. For the same topology and the same strut thickness of the lattice structures, the porosity increases as the unit cell size increases. This indicates that, for the same topology, the lattice structures of larger cell sizes with thinner strut thicknesses provide larger pore sizes leading to larger porosities.

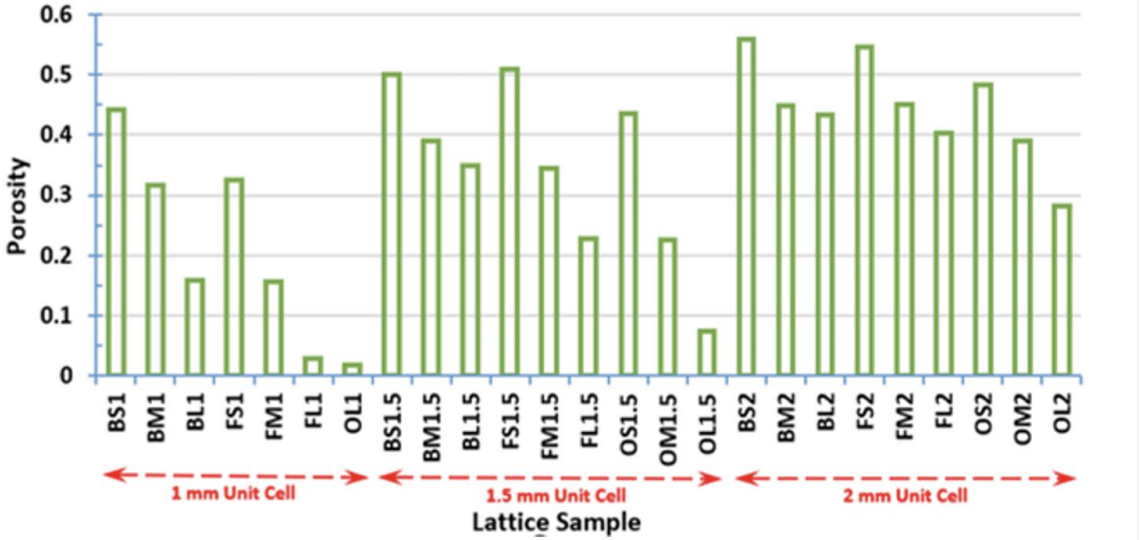

Fig. 6 Porosity measurements for lattice samples of different topologies, cell sizes, and strut thicknesses.

Rate of Rise Results

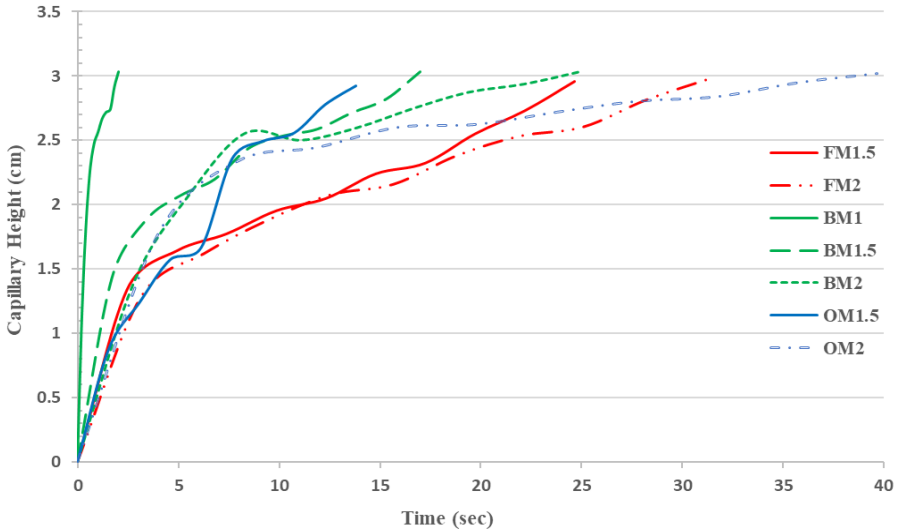

Fig. 7 Capillary displacement against time for several representative lattice samples of different topologies and cell sizes with the same strut thickness labeled by "M".

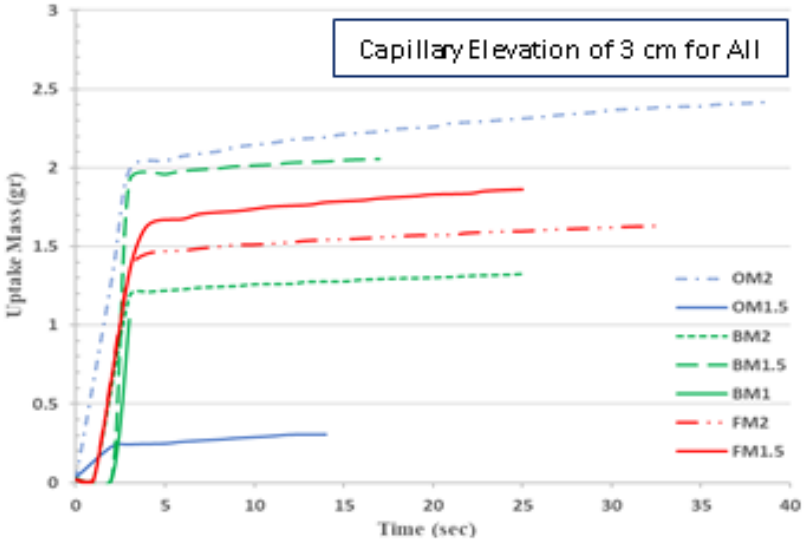

Fig. 8 Uptake/wicked mass against time for several representative lattice samples as another adaptation to the capillary rate-of-rise tests.

- Fig. 7 illustrates the rate-or-rise capillary elevation of methanol as a function of time: once the lattice sample is first brought into contact with the liquid, the working fluid of methanol rises very quickly at the early stages of the capillary rising process, indicating that the capillary driving force is much greater than the flow hydraulic resistance and the gravity effect, which causes the meniscus front in the wick samples to have a fast-rising velocity.

- A similar observation is found in Fig. 8: after the early stages of the wicking process which takes less than 5 seconds for all the lattice samples, the wicked mass rate drops significantly with time. The declining slopes of the samples for the capillary height rate can also be witnessed after 5 seconds in Fig. 7.

Permeability and Effective Pore Radius

- Fig. 9 displays such an analysis for a representative lattice sample of BM1.5. As illustrated in Figs. 9(a) and 9(b), a minimum mean absolute percent deviation of 0.003% points simultaneously to an effective pore radius of 183 μm and a permeability value of 113 $\mu m2$, respectively.
- Fig. 10 shows two lattice samples of FM1.5 and BL1.5 are found to have almost the same permeabilities where both have almost the same porosities (i.e., 0.345) and pore openings (i.e., 500 μm), indicating that the permeability is predominantly a function of porosity and pore size.

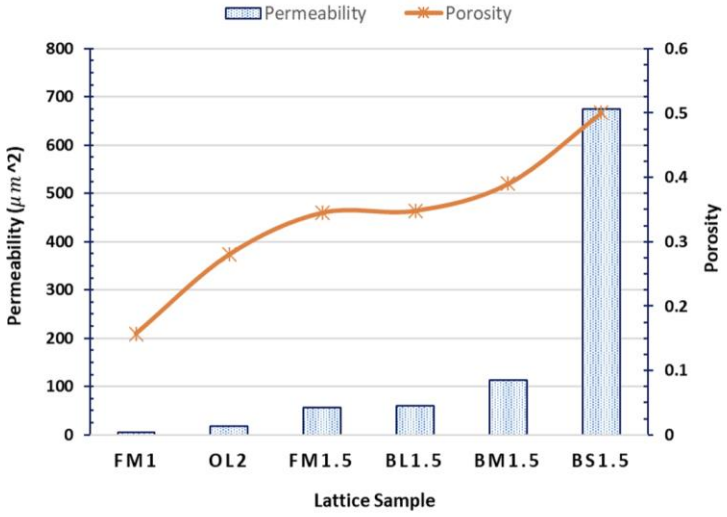

Fig. 10. Permeability measurements for several lattice samples along with their corresponding porosities.

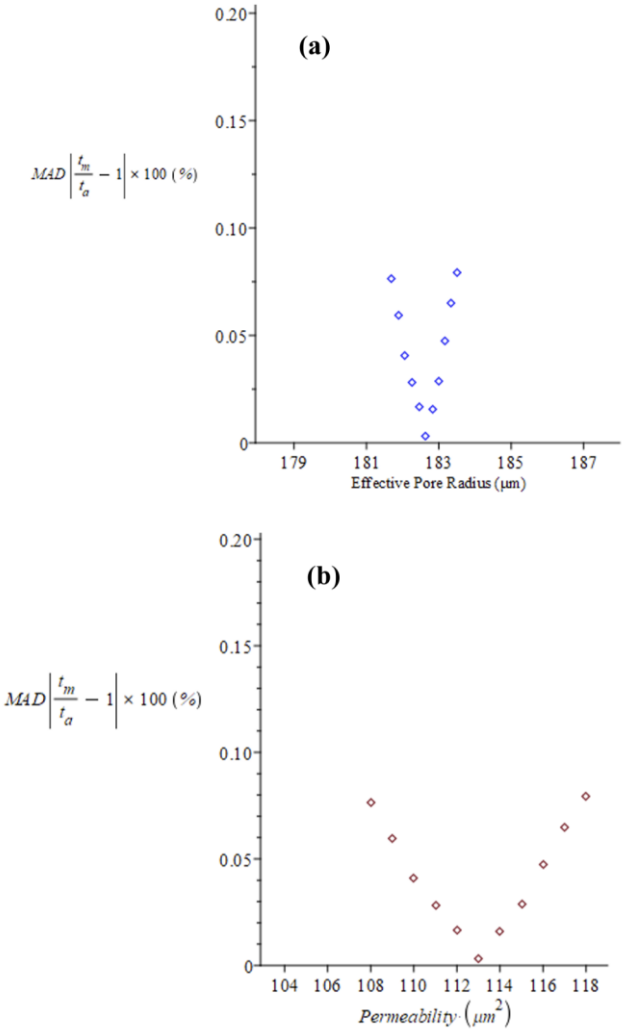

Fig. 9. Representative data analysis performed for the lattice sample BM1.5 using experimental measurements of porosity and rate-of-rise tests to estimate a) effective pore radius, and b) permeability at the minimum mean absolute percent deviation (MAD) of 0.003%.

Manufacturing Challenges Observed

- The results consistently reveal higher porosities for the body-centered cubic topology compared to those of the face-centered cubic and octet truss, respectively, for the same unit cell size and the same strut thickness.

- However, specimens with a higher number of struts were more likely to experience blockages. This was only exaggerated as the strut sizes got larger and the unit cell sizes got smaller.

- As shown here in Fig. 11, by design the strut size is 0.3 mm but after manufacturing the measured size is 0.38 mm. This maybe contributed to the fact that this could be attributed to over melting of the structure since default parameters were used to make these structures as shown in Fig.12.

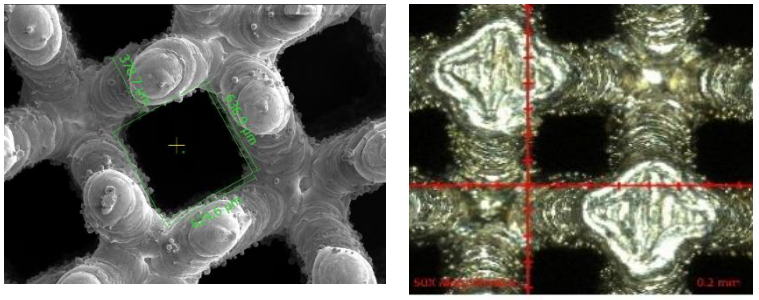

Fig. 11 SEM photo of specimen BL1.5, and Optical micrographs of lattice samples: a)*BL1.5* with pore opening of 500 μm,

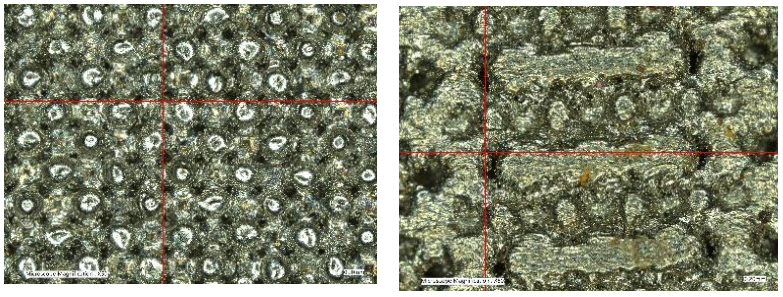

Fig. 12 Over melting of strut size of lattice structures for OL1 & OL1_5

Conclusions

- In this study, lattice structures of different cell topologies, cell sizes, and strut thicknesses were additively fabricated with Maraging Steel using the Direct Metal Laser Sintering (DMLS) technique.
- Furthermore, the key porous properties and capillary characteristics of the printed wick structures, including porosity, capillary height and mass rates, and permeability, were experimentally characterized and compared for the working fluid of methanol as commonly used for passive two-phase heat exchangers in space applications.
- Due to the difficulty generally faced in locating the meniscus front in lattice structures without armed eyes which can affect the reliability of data, this work took advantage of an infrared (IR) camera to properly distinguish the front location while simultaneously measuring the changes in liquid mass wicked into the lattice samples over time to show another adaptation to the classical capillary rate-of-rise tests.
- From the present study, it was generally observed that the lattice samples with the body-centered cubic topology exhibit better porosities and permeabilities with higher rates of capillary height and uptake mass compared to those with the other two topologies consisting of faced-centered cubic and octet truss.

Acknowledgments

The authors gratefully acknowledge financial support from NASA MUREP Institutional Research Opportunity Grant under Cooperative Agreement #80NSSC19M0196 as well as the financial support from the Department of Defense (DOD) via contract #W911NF2010274.

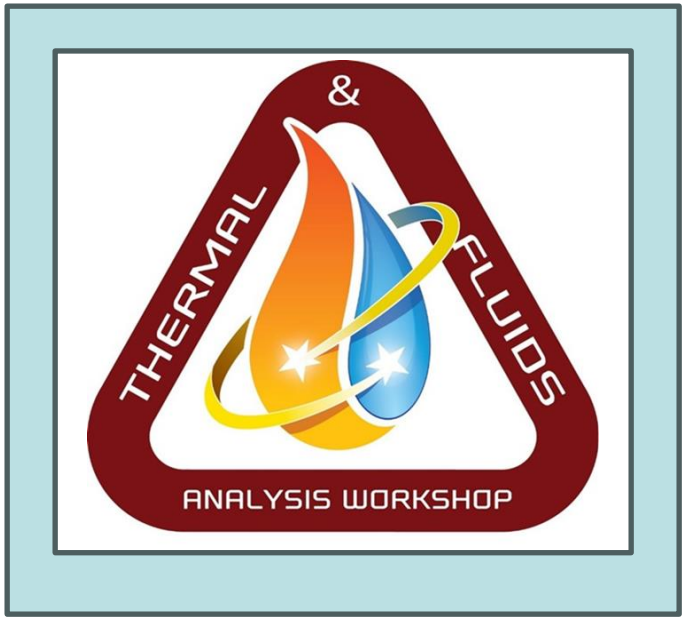

Many Thanks!
Questions?
Comments?